

CALCULATION AND INTERPRETATION OF HADRON
CORRELATION FUNCTIONS IN LATTICE QCD*

M. Burkardt‡, J. M. Grandy† and J. W. Negele

*Center for Theoretical Physics
Laboratory for Nuclear Science
and Department of Physics
Massachusetts Institute of Technology
Cambridge, Massachusetts 02139 U.S.A.*

Submitted to: *Annals of Physics*

CTP#2109

hep-lat/9406009

May 1994

* This work is supported in part by funds provided by the U. S. Department of Energy (D.O.E.) under contracts DE-FG06-90ER40561, DE-FG06-88ER40427, and DE-FC02-94ER40818.

‡ Present address: Institute for Nuclear Theory, University of Washington, Seattle WA 98195

† Present address: MS B-285, Los Alamos National Laboratory, Los Alamos NM 87545

ABSTRACT

Several new developments in the calculation and interpretation of hadron density-density correlation functions are presented. The asymptotic behavior of correlation functions is determined from a tree diagram path integral. A method is developed to use this behavior to correct for leading image contributions on a finite periodic spatial lattice and to correct for the finite temporal extent of the lattice. Equal time correlation functions are shown to determine a sum of the ground state rms radius plus a polarization correction, and it is shown how to extract the hadron polarizability from unequal time correlation functions. Image-corrected correlation functions calculated in quenched lattice QCD are presented and used to determine the size of the pion and nucleon.

I. INTRODUCTION

One of the primary motivations for solving QCD on a lattice is to understand the structure of hadrons. Hence, in addition to reproducing the hadron spectrum and experimentally measured form factors, it is important to explore the spatial distributions of quarks and the correlations between them in the ground states of hadrons. As in other strongly interacting many-body systems, two-body correlation functions are a natural starting point, with the simplest being the density-density correlation function

$$\rho(\vec{y}, t_1, t_2) \equiv \int d\vec{x} \langle h | \bar{u}_{\vec{x}, t_1} \gamma^0 u_{\vec{x}, t_1} \bar{d}_{\vec{x}+\vec{y}, t_2} \gamma^0 d_{\vec{x}+\vec{y}, t_2} | h \rangle \quad (1.1)$$

where $|h\rangle$ denotes a hadronic ground state and u and d represent field operators for up and down quarks respectively. Although these correlation functions have been studied in a number of works [1–4], several important practical and conceptual problems were previously unresolved and errors were made in interpreting correlation functions. Hence, this work presents a number of new results relevant to the calculation and interpretation of density-density correlation functions.

One practical problem surrounding all lattice QCD calculations is the irreconcilable conflict with finite computer resources between reducing the lattice spacing (and thus accurately approximating the continuum limit) and increasing the physical volume of the lattice (and thus eliminating finite volume corrections). Nowhere is the conflict more severe than in the calculation of density-density correlation functions in hadrons. Conventional hadron wave functions, either gauge fixed in Coulomb or Landau gauge or made gauge invariant by a line of flux $e^{i \int dx A}$, fall off much more rapidly than quark correlation functions because they contain additional suppression factors at large separation arising from the small overlap between the gluon wave functional in the hadron and in the vacuum [5]. Typically the spatial extent of these wave functions is half that of the density-density correlation functions, so that lattices in common use which are adequate for wave functions are much too small for correlation functions [3].

In section 2, we therefore take a fresh look at the general problem of relating correlation functions in a periodically replicated array of hadrons, corresponding to periodic boundary conditions on a spatial lattice, to those in an isolated hadron. We begin with a pedagogical example in one spatial dimension and show how to correct for the effects of periodic images and generalize to the physical case of three space dimensions. A crucial ingredient in obtaining the properties of an isolated hadron is understanding the asymptotic decay of the correlation functions. Since the behavior is more complicated than simple exponential decay governed by the rho mass, in section 3 we construct a tree diagram path integral which incorporates the essential physics. This path integral accurately describes the asymptotic behavior and provides a means to remove finite spatial and temporal volume effects. It also explains an apparent paradox wherein two seemingly equivalent methods of calculating correlation functions yielded different asymptotic behavior [6].

Given the possibility of accurately determining the density-density correlation function for an isolated hadron, it is important to understand clearly its physical content and to explore the full range of physical information which can be extracted from it. For this reason, in section IV we reexamine the physical content of the density-density correlation functions at equal and unequal time in the nonrelativistic limit, which is particularly simple to understand. We show that the rms radius of the equal time correlation function is not the rms radius of the hadron, as previously claimed, but rather is the sum of the rms radius and a dipole-dipole polarization term. Furthermore, we show how to extract the hadron polarizability from integrating the correlation function over relative time, and generalize the results to the relativistic case and more general currents.

Finally, having developed the general formalism and methodology, the results of quenched lattice calculations for density-density correlation functions for the π , ρ and nucleon are presented and discussed in section V. The conclusions and outlook are discussed in section VI.

II. PERIODIC IMAGES IN LATTICE GAUGE THEORIES

Intuitively, it is clear that when we calculate hadron correlation functions in a finite spatial volume with periodic boundary conditions, we are not considering an isolated hadron but rather a periodically replicated array of hadrons. Consequently, periodicity effects and interactions between neighboring hadrons will occur and we either must discover how to correct for these effects or calculate with a volume so large that these effects are negligible.

The primary result we will establish in this section is that the density-density correlation function for a gauge theory on a periodic lattice of spatial dimension L has the form

$$\rho_{\text{periodic}}(\vec{r}) = \sum_{\vec{n}} \rho_0(\vec{r} + \vec{n}L) \quad (2.1)$$

where $\rho_0(\vec{r})$ is an accurate approximation to the free hadron result $\rho(\vec{r})$ for $r < L$ and differs due to interactions with periodic images only for $r \gtrsim L$. This result embodies two physically distinct effects. The dominant effect of periodicity is just the summation of the tails of ρ_0 from neighboring images, and this effect amounts to a factor of 2 correction at distance $\frac{L}{2}$ along the Cartesian axes. The second effect is the discrepancy between ρ_0 and ρ arising from interactions with periodic images, and it first appears at distance L . Fortunately, since the dominant effect is the sum of tails from images, it can be removed by subtracting these image contributions, leaving only the residual discrepancy between ρ_0 and ρ beyond $r \approx L$ which will be negligible in cases of practical interest.

To understand how the form (2.1) arises in a gauge theory and how ρ_0 may be obtained by subtracting image contributions, it is useful to begin by considering the simple example of QED coupled to non-relativistic particles in 1 + 1 dimensions on a circle.

Positronium on a circle

In the continuum, using the gauge $\partial_x A_x = 0$, the Hamiltonian for a non-relativistic e^+e^- pair in 1 + 1 dimensions on a circle with circumference L is

$$H = -\frac{1}{2L} \frac{d^2}{dA_x^2} + \frac{(p_1 - eA_x)^2}{2m} + \frac{(p_2 + eA_x)^2}{2m} + V(x_1 - x_2) \quad (2.2)$$

where $V(x)$ is the periodic potential

$$\begin{aligned}
V(x) &= \frac{e^2}{2\pi} \frac{L}{2\pi} \sum_{\substack{n=-\infty \\ n \neq 0}}^{\infty} \frac{1 - e^{\frac{2\pi i x n}{L}}}{n^2} \\
&= \frac{e^2}{2} |\tilde{x}| \left(1 - \frac{|\tilde{x}|}{L} \right) \quad , \quad \tilde{x} = |x|_{\text{mod } L}
\end{aligned} \tag{2.3}$$

The Schrödinger equation corresponding to H , Eq. (2.2), must be solved with appropriate boundary conditions on the wavefunction. Here we will use periodic boundary conditions in x_1 and x_2

$$\psi(x_1 + L, x_2, A_x) = \psi(x_1, x_2 + L, A_x) = \psi(x_1, x_2, A_x) \tag{2.4}$$

although other boundary conditions are also possible. The center-of-mass motion separates in Eq. (2.2), *i.e.*

$$H = -\frac{1}{2L} \frac{d^2}{dA_x^2} + \frac{P^2}{4m} + \frac{(p - eA_x)^2}{m} + V(x) \tag{2.5}$$

where $P = p_1 + p_2$, $p = (p_1 - p_2)/2$, $x = x_1 - x_2$. Notice that Eq. (2.4) implies periodicity in the center-of-mass and the relative coordinate separately. The eigenstates of H corresponding to $P = 0$ can be expressed in the form

$$\psi_k(x, A_x) = \sum_n e^{i(x-nL)A_x \cdot e} \hat{\psi}_k(x - nL) \quad . \tag{2.6}$$

where $\hat{\psi}_k$ is a solution of the equation

$$E_k \hat{\psi}_k(x) = \left(\frac{p^2}{m} + \hat{V}(x) \right) \hat{\psi}_k(x) \quad , \tag{2.7}$$

with

$$\hat{V}(x) = V(x) + \frac{e^2}{2L} x^2 \quad . \tag{2.8}$$

Note that $\psi(x, A_x)$ is defined only for $-L < x < L$ (with periodic or quasiperiodic boundary conditions), whereas $\hat{\psi}(x)$ is defined for $-\infty < x < \infty$ (with vanishing boundary conditions). This difference in domain allows a function of one variable to carry the same information as a function of two variables.

For $x = nL + \Delta x$, where $n \in \mathbb{N}$ and $0 < \Delta x < L$, the effective potential \hat{V} can be rewritten in the form

$$\hat{V}(x) = \frac{e^2}{2L}(nL)^2 + (2n+1)\frac{e^2}{2}\Delta x \quad , \quad (2.9)$$

which allows a simple physical interpretation. Consider the case in which the e^+ moves around the circle n times while the e^- is fixed. The electric flux from the e^+ to the e^- ends up in a configuration where it is wrapped around the circle n times, since there are no terms in the Hamiltonian which would allow the gauge field to make a transition to the energetically lowest unwrapped configuration. The electric field energy density is proportional to the electric field strength squared — the latter being $(n+1) \cdot e$ for $0 < x < \Delta x$ and ne for $\Delta x < x < L$ in the above example. Hence

$$E_{\text{gauge}} = \frac{1}{2} \left\{ \Delta x \cdot [(n+1)e]^2 + (L - \Delta x)[ne]^2 \right\} \quad (2.10)$$

which agrees with Eq. (2.9).

Note that for $-L < x < L$ the effective potential (which determines the excitation spectrum of H) agrees with the potential on a line, *i.e.* $\hat{V}(x) = \frac{e^2}{2}|x|$. In contrast, if we had omitted the A_x degree of freedom, we would have obtained ($|x| < L$)

$$V(x) = \frac{e^2}{2}|x| \left(1 - \frac{|x|}{L} \right) \quad , \quad (\text{periodic}) \quad (2.11)$$

which is a much worse approximation to $\frac{e^2}{2}|x|$ than Eq. (2.9). Although the A_x degree of freedom “freezes out” for $L \rightarrow \infty$ (see Eq. (2.5)), its presence improves the approach to the infinite volume result for finite L .

For $|x| > L$, the interaction is modified by the periodic boundary condition. In a sense the positronium interacts with its own periodic replicas. However, in most cases, this has only an exponentially suppressed effect on energy eigenvalues and the wavefunctions, since the wave functions fall off exponentially for large x .

For ground state correlations another finite size effect is of much more importance. Consider

$$\rho_k(x) \equiv \int dy \langle k | \delta(x_1 - y) \delta(x_2 - x - y) | k \rangle \quad , \quad (2.12)$$

where $|k\rangle$ denotes the k^{th} positronium state. Using Eq. (2.6),

$$\begin{aligned}
\rho_k(x) &\propto \int dA |\psi_k(A, x)|^2 = \sum_{n,m} \int dA e^{i(mL-nL)eA} \hat{\psi}_k(x-nL) \hat{\psi}_k^*(x-mL) \\
&= 2\pi \sum_{n,m} \delta(nL-mL) \hat{\psi}_k(x-nL) \hat{\psi}_k^*(x-mL) \\
&\propto \sum_n \hat{\rho}_k(x-nL) \quad ,
\end{aligned} \tag{2.13}$$

where

$$\hat{\rho}_k(x) = \left| \hat{\psi}_k(x) \right|^2 . \tag{2.14}$$

The essential result is that the interference terms ($\propto \hat{\psi}_n \hat{\psi}_m^*$, $n \neq m$) are removed by the integration over A .*

Equation (2.13) shows explicitly how the general result, Eq. (2.1), arises in $1+1$ dimensions, gives a precise definition of ρ_0 as $\hat{\rho}_k$, and displays the role the gauge field plays in obtaining this result. The longitudinal gauge field A_x , which is the only quantum mechanical degree of freedom associated with the gauge field in QED_{1+1} , plays two essential roles. First, it removes all cross terms so only the square of the wave function $|\tilde{\psi}_k(x)|^2$ appears in the final result. Secondly, it replaces the periodic potential, Eq. (2.11), by the linear potential in the range $-L < x < L$, so that $\tilde{\psi}_k(x)$ satisfies the correct Schrödinger equation in this entire range. The role of A_x has also been emphasized by a number of authors in the context of the Schwinger model [7], where it turns out to be crucial in providing a proper description of the anomaly in the divergence of the axial vector current.

A numerical example in 1+1 dimensions

To show how the density for a free bound state, $\rho_0(x)$, may be extracted from the periodic sum $\rho_{\text{periodic}}(x)$ in Eq. (2.1), we now consider a numerical example. For convenience,

* To avoid irrelevant details, we have not been explicit about normalization and the $\delta(0)$ -term ($m = n$ in Eq. (2.13)) arising because we work in the continuum. In a lattice calculation, the gauge field integration is compact.

and to establish contact with the lattice formulation of QCD_{3+1} , we use a discrete lowest order difference approximation to the Hamiltonian, Eq. (2.7). Note that beginning with QED_{1+1} lattice gauge theory and gauge fixing analogously yields an equivalent form with one quantum mechanical gauge degree of freedom remaining [8,9]. The general conclusion will be independent of the discretization.

To emphasize the image corrections, we have chosen the example shown in Fig. 1, in which there is greater overlap between the bound state and its periodic images than in a typical lattice QCD calculation. Note that the periodic solution, denoted by the heavy solid curve, falls to less than half of its peak value. This case has $N = 10$ lattice sites separated by spacing a , with mass $ma = 0.3$ and charge $ea = 0.3$. With these parameters, the exact solution on the open line, shown by the light solid curve, has size $\sqrt{\langle r^2 \rangle} \simeq 3.6a$.

Our general strategy for image corrections is to use the known asymptotic decay of the infinite domain solution both to subtract the tails of the first images in the fundamental unit cell and to approximate the solution outside the unit cell. Thus, in any dimension, assuming the asymptotic form $\rho_{\text{as}}(\vec{r})$ is known, the image corrected density $\rho_{\text{cor}}(\vec{r})$ is defined

$$\rho_{\text{cor}}(\vec{r}) = \rho_{\text{as}}(\vec{r}) \tag{2.15a}$$

for \vec{r} outside the fundamental unit cell and

$$\rho_{\text{cor}}(\vec{r}) = \rho_{\text{periodic}}(\vec{r}) - \sum_{\vec{n} \neq 0} \rho_{\text{as}}(\vec{r} + \vec{n}L) \tag{2.15b}$$

for \vec{r} inside the first unit cell.

In our one-dimensional example, we make use of the known asymptotic behavior for Airy functions, so that as $a \rightarrow 0$, the density has the form

$$\rho_{\text{as}}(x) \sim \exp\left(-\lambda x^{3/2}\right) \quad , \quad \text{where} \quad \lambda = \frac{4}{3} \sqrt{\frac{me^2}{2}} \quad . \tag{2.16}$$

In the continuum limit, with the above parameters, $\lambda = 0.155$. For finite lattice spacing, λ is somewhat smaller. The normalization of $\rho_{\text{as}}(x)$ is determined by the symmetry condition

$$\rho_{\text{as}}\left(\frac{L}{2}\right) = \frac{1}{2} \rho_{\text{periodic}}\left(\frac{L}{2}\right) \tag{2.17}$$

Although, by construction, $\rho_{\text{cor}}(x)$ and its first derivative are continuous at $x = \pm \frac{L}{2}$, its second derivative is not, both because of finite a corrections to λ and because $\rho(x)$ is not yet asymptotic at $x = \pm \frac{L}{2}$. Especially when one is also interested in the Fourier transform, it is desirable to parameterize the image corrections such that the second derivative is continuous, and there are several possibilities. One possibility is simply to define λ such that $\rho_{\text{cor}}(x)$ also has a continuous second derivative. Alternatively, one may make the *ansatz*

$$\rho_{\text{as}}(x) \sim (a + bx) \exp\left(-\lambda x^{3/2}\right) \quad (2.18)$$

and determine b/a by the same criterion. Since there are polynomial corrections to Eq. (2.16), this form is clearly reasonable. The results are essentially the same, and we only show calculations using the *ansatz* (2.18).

The result of correcting the periodic solution using Eq. (2.15) with the asymptotic form Eq. (2.18) with $\lambda = 0.13$ is shown by the dashed line in Fig. 1. This corrected result agrees quite well with the exact solution on the infinite domain, shown by the light solid line, especially considering the high degree of overlap in our deliberately chosen worst-case example. Note that the reconstruction of the density is not extremely sensitive to the precise value of λ . Although the discrete solution on the open line yields $\lambda \approx 0.145$, the value $\lambda = 0.13$ we have chosen and $\lambda = 0.15$ used in calculations which are not shown here yield very similar results.

The Fourier transforms of the densities in Fig. 1 are shown in Fig. 2. We will show in Section IV that they are the sums of squares of elastic and inelastic form factors. The Fourier transform of the periodic density is only defined at the discrete lattice momenta $q_k = k\pi/L$ and is indicated by the solid dots in Fig. 2. An equivalent way of rephrasing our image correction problem is to ask whether we can use our knowledge of the form of the density, Eq. (2.1) and the asymptotic behavior to reconstruct the Fourier transform for all qa . Clearly, the curvature at the origin, for example, is related to the rms radius of the correlation function and must depend sensitively on the details of the surface in a

way which cannot be guessed by naive polynomial interpolation of the solid points. One observes that the Fourier transform of the corrected density from Fig. 1, denoted by the solid curve in part (a), agrees well with the Fourier transform of the exact result on the open line. We should emphasize that the level of agreement shown in part (a) of Fig. 2 and in Fig. 1 is not unique to the particular set of parameters we have chosen, and that similar results were obtained for a wide range of parameters N , ma , and ea .

The importance of making the second derivative of the corrected density continuous is shown by comparing curves (a) and (b) of Fig. 2. The solid curve (b) shows the result of using Eq. (2.16) for the asymptotic tail with the same value $\lambda = 0.13$ but not introducing an additional linear term as in Eq. (2.18) which can be used to make the second derivative continuous. The substantial oscillations around the exact result show how large the effects from the discontinuity become at intermediate values of qa . One should note that Eq. (2.1) has the property that at the discrete lattice momenta $q_k = k\pi/L$, the Fourier transforms of ρ_{periodic} and ρ_0 are identical, so that to the extent that second and higher image corrections are negligible, both the solid and dashed lines must go through the solid dots.

In practical lattice calculations, the periodic signal $\rho_k(x)$ in Eq. (2.13) is not a smooth function but rather is contaminated with statistical noise. This adds another level of complication to the reconstruction of $\rho_{\text{cor}}(x)$. To study this case, in part (c) of Fig. 2 we have considered an ensemble of 10 data sets obtained by adding randomly distributed errors with mean fractional deviation 1% to the periodic density at each lattice site. As before, for the matching conditions we use continuity of ρ and the second derivative. Instead of using a three-point formula, both are now computed using a five-point formula which automatically provides some averaging over the statistical fluctuations. One observes that for $q < \pi/L$ the resulting form factor turns out to be quite stable, and one has as before an accurate determination of the rms radius. However, as expected, for larger values of q at which the Fourier transform has fallen by two orders of magnitude, the 1% errors introduce uncertainties comparable to the signal. In this region, the uncertainty is well represented by the variance of the solid dots coming from the periodic solution and no further information can be obtained by image corrections.

Image Corrections in QCD_{3+1}

Fortunately, although one cannot carry through an explicit solution as in the case of QED_{1+1} , Eq. (2.1) also applies to QCD_{3+1} with periodic boundary conditions in the spatial direction. The effects of images may be understood by considering all possible contractions of the field operators occurring in all periodic replicas of the density operators and all periodic replicas of the sources.

Representative contractions relevant to meson density-density correlation functions are sketched in Fig. 3, where one periodic spatial dimension x is shown on a cylinder and the other two spatial dimensions are suppressed. The circumference of the cylinder is L , and the separation between the two density operators on the midplane of the cylinder measured on the front of the cylinder is denoted r and around the back of the cylinder is $|r - L|$. The upper sketch shows the case in which all contractions occur within the fundamental unit cell and yields the physical result in the infinite volume limit. The middle sketch shows a typical contraction in which the meson is created in the fundamental unit cell on the left creating the wave function $\psi_0(r)$ at the midplane whereas on the right, a propagator from the first periodic image creates the wave function $\psi_0(r - L)$ at the mid plane. For a periodic wave function which could be written in the form $\psi(\vec{r}) = \sum_n \psi_0(\vec{r} + \vec{n}L)$, this contraction would thus correspond to a cross term of the form $\psi_0(\vec{r} + \vec{n}L) \psi_0(\vec{r} + \vec{m}L)$. Clearly, if this term were non-vanishing, one would never obtain the form Eq. (2.1) which is just the sum of diagonal terms. However, since the total propagator in the middle sketch has the topology of a spatial Polyakov line, it therefore vanishes in the confining phase for a sufficiently large lattice. This is the physical reason no cross terms occur in gauge theories in any dimension. Finally, the bottom sketch shows a typical contraction in which the meson is created with propagators from the first periodic image on the left and on the right, corresponding to the diagonal term $\psi_0(r - L) \psi_0(r - L)$, giving rise to a diagonal contribution to the density of the form $\rho(r + nL)$. Extending this argument to all contractions in 3+1 dimensions, one can see that the Polyakov line argument removes all cross terms, and that the result must have the form of Eq. (2.1).

Thus, in principle, the procedure for correcting images in higher dimensions is completely analogous to that in two dimensions. However, from the practical point of view there is an additional complication since the boundary of a cube in $D > 1$ dimensions is a $D - 1$ -dimensional extended object and it would be very difficult to impose continuity everywhere on the boundary. Therefore, it is useful to consider more general matching conditions to replace the continuity requirement.

To this end, it is important to note that there are only a few critical points on the boundary where it is essential to achieve continuity. This can be seen by calculating the angular averaged form factor

$$\tilde{\rho}(q) = \int d\Omega_q \tilde{\rho}(\vec{q}) \propto \int_0^\infty dr r^{D-1} \frac{\sin qr}{qr} \rho(r) \quad , \quad (2.19)$$

where

$$\rho(r) = \int d\Omega_r \rho(\vec{r}) \quad . \quad (2.20)$$

Obviously, if one wants to avoid unphysical oscillations in $\tilde{\rho}(q)$, one should keep $\rho(r)$ as smooth as possible. In order to see what conditions this implies for $\rho(\vec{r})$, consider the extreme case of a step function in two dimensions ($\vec{r} = (x, y)$)

$$\rho(\vec{r}) = \begin{cases} 0 & |x| > a \text{ or } |y| > a \\ 1 & |x| < a \text{ and } |y| < a \end{cases} \quad , \quad (2.21)$$

yielding, after taking the angular average,

$$\rho(r) = \begin{cases} 1 & 0 \leq r \leq a \\ 1 - \frac{4}{\pi} \sin^{-1} \frac{r}{2a} & a < r < a \cdot \sqrt{2} \\ 0 & r \geq a \cdot \sqrt{2} \end{cases} \quad (2.22)$$

Note that although $\rho(\vec{r})$ is discontinuous everywhere on the boundary of the square, $\rho(r)$ and its derivatives are continuous everywhere except at two critical points: $r = a$ and $r = \sqrt{2}a$, where $\rho'(r)$ is discontinuous. Physically, this corresponds to that fact that when one increases r and the sphere $|\vec{r}| = r$ intersects with the corner or the center of the faces of the square (Eq. (2.22)) then there is a sudden change in the fraction of the

sphere contained inside the square, reflected in a discontinuous derivative. Turning now to three dimensions, we see that if we need to match solutions inside and outside the cubic unit cell where discontinuities can occur only at the boundary, discontinuities in $\rho(r)$ or its derivative will arise only if $\rho(\vec{r})$ is not continuous in the corners, the center of the edges, or the center of the faces of the first unit cell. Hence, unphysical oscillations in the form factor at large q are avoided most efficiently if the parameters of the asymptotic density, such as in Eq. (2.18), are determined such that the discontinuities around these critical points are minimized.

In the practical case of lattice calculations in which the density measured at every point has statistical errors, a different strategy is required, and an iterative self-consistent method to determine the optimal density is described in section V.

III. THE ASYMPTOTIC BEHAVIOR OF DENSITY-DENSITY CORRELATIONS

In the last section we showed how one can use the knowledge of the asymptotic behavior of the density for an isolated hadron, $\rho_0(\vec{r})$, to correct for images in the density of a periodic system, related to ρ_0 by

$$\rho_{\text{periodic}}(\vec{r}) = \sum_{\vec{n}} \rho_0(\vec{r} + \vec{n}L) \quad . \quad (3.1)$$

Hence, because our ultimate objective is to study lattice measurements of physical correlation functions, we will show in this section how to determine the behavior at large separation $|y|$ of the pion density correlation function:

$$\begin{aligned} \rho(\vec{y}, t_1, t_2) &\equiv \sum_{\vec{x}} \langle \pi | \rho^u(\vec{x}, t_1) \rho^d(\vec{x} + \vec{y}, t_2) | \pi \rangle \\ &= \sum_{\vec{x}} \sum_n \langle \Omega_n | J^+(\vec{r}_{\text{out}}, T) \rho^u(\vec{x}, t_1) \rho^d(\vec{x} + \vec{y}, t_2) J(\vec{r}_{\text{in}}, 0) | \Omega_n \rangle \end{aligned} \quad (3.2)$$

where the up quark density operator is $\rho^u(\vec{x}, t) \equiv: \bar{u}_{\vec{x},t} \gamma^0 u_{\vec{x},t} :$, ρ^d is the corresponding operator for down quarks, $J(\vec{x}, t)$ is the pion source $\bar{u}_{\vec{x},t} \gamma_5 u_{\vec{x},t}$, $\{\Omega_n\}$ denotes states

with the quantum numbers of the vacuum, \vec{r}_{in} and \vec{r}_{out} denote the positions of the pion sources, and we work in Euclidean time. The analysis of the hadron correlation function is analogous.

We will use the fact that at large distances, QCD is dominated by light hadrons to motivate a tree graph approximation to the asymptotic correlation function. Consider a typical time history for the pion correlation function $\rho(\vec{y})$ shown in the left portion of Figure 4, where for simplicity we consider the equal time case $t_1 = t_2 = t$. In the quenched approximation, one has a $u\bar{d}$ quark-antiquark pair connecting the sources J, J^+ and the density operators ρ^u and ρ^d as shown by wiggly lines, interacting via the exchange of gluons which are suppressed in the figure. Physically, at large Euclidian separation we expect the interacting quark-antiquark pairs to form meson ground states in the appropriate channels, so that the quark-level time history in the left sketch is replaced by the corresponding meson tree graph shown at the right. As long as each meson propagator is of sufficient length, this approximation should be accurate. Formally, the same result may be obtained by inserting complete sets of meson states between each of the operators and identifying the leading singularities [10]. In either case, since the sources couple to the π and the external currents couple to the ρ , the tree-graph approximation to the correlation function Eq. (3.2) yields

$$\begin{aligned} \rho_{\text{tree}}(\vec{y}) = & \sum_{\vec{x}} \sum_{\vec{r}_1, \vec{r}_2} D_\pi(\vec{r}_1 - \vec{r}_{\text{in}}) D_\pi(\vec{r}_2 - \vec{r}_1) D_\pi(\vec{r}_{\text{out}} - \vec{r}_2) \\ & \times g_{\rho\pi\pi} D_\rho(\vec{x} - \vec{r}_1) g_{\rho\pi\pi} D_\rho(\vec{x} + \vec{y} - \vec{r}_2) + (\text{“1} \leftrightarrow \text{2”}) \quad , \end{aligned} \quad (3.3)$$

where for simplicity we use lattice propagators for scalar mesons [11] for the D 's. In practice, to evaluate this expression on a lattice for comparison with lattice QCD results, it is preferable to Fourier transform to momentum space and perform the sums over discrete lattice momenta.

A further approximation to the sum over tree graphs in Eq. (3.3) which provides insight into the asymmetric behavior is given by the stationary or classical approximation in which instead of summing over all joint positions r_1 and r_2 , we select only those joints in which

the product of propagators takes on maximal values. Replacing the lattice propagator by a simple continuum exponential $D(\vec{r}) \rightarrow e^{-m r}$, we obtain

$$\rho_{\text{stationary}}(\vec{y}) = \sum_{\vec{x}} (\rho_{\rho\pi\pi})^2 \max_{\vec{r}_1, \vec{r}_2} e^{-m_\pi |\vec{r}_1 - \vec{r}_{\text{in}}|} e^{-m_\pi |\vec{r}_2 - \vec{r}_1|} e^{-m_\rho |\vec{x} - \vec{r}_1|} e^{-m_\rho |\vec{x} + \vec{y} - \vec{r}_2|} e^{-m_\rho |\vec{r}_{\text{out}} - \vec{r}_2|} \quad (3.4)$$

Here $|\cdot|$ denotes the Euclidean distance and $r_{\text{in}} = (0, \vec{0})$, $r_{\text{out}} = (T, \vec{0})$, and $x = (t_1, \vec{x})$. The physical picture that results depends on the numerical value of the ratio m_π/m_ρ .

The asymptotic behavior of pion correlation functions calculated in lattice QCD and in the tree-level approximation are compared in Fig. 5. Although the lattice calculations are discussed in detail later in Section 5, at this point the only information that is needed is the fact that calculations were performed at three values of the hopping parameter κ corresponding to the hadron masses given in Table I. For the heaviest quark mass case, κ_2 , m_π is only 27% below m_ρ and for the lightest case, κ_5 , m_π is slightly above $\frac{1}{2}m_\rho$.

One important result seen in Figure 5 is the fact that beyond 1 fm, the tree-level approximation accurately describes the behavior of the lattice QCD results denoted by the solid curves. The tree-level results at selected points before image corrections are shown by the squares: Three interior points for which image corrections are negligible, are denoted by solid squares, and results at all other points which are subject to image effects are denoted by open squares. By symmetry, image contributions at the center of the faces, center of the edges, and corners of the first unit cell may be subtracted by dividing by 2, 4, and 8 respectively, and the results so corrected are denoted by the solid octagons. Thus, all the solid symbols are free of image effects and are seen to agree extremely well with the solid lattice QCD curves as claimed. For the purpose of this comparison, the image-corrected tree level results were normalized to agree with the lattice results at $r/a = 14$.

Another significant feature observed in Fig. 5 is the fact that in the region of 1-2 fm, the slope does not approach a fixed value given by a meson mass. Rather, it gradually changes in this region, taking on values intermediate between exponential decay with m_ρ and m_π indicated by the dotted lines in the figure. At first, this may seem surprising,

since because the current couples to the ρ , one might naively expect the asymptotic decay of the correlation function at large distances to decay as $e^{-m_\rho y}$.

The behavior of the asymptotic slope may be understood qualitatively using the stationary approximation to the tree-diagram sum. A useful way to state the stationary condition for the joints \vec{r}_1 and \vec{r}_2 in Fig. 4 is to connect all the vertices by classical strings, weight the length of each string segment by the corresponding meson mass, and minimize the total energy of these classical strings. In this approximation, it is simple to determine the asymptotic behavior in various regimes of interest.

First, consider the case $m_\pi < \frac{1}{2}m_\rho$, which corresponds to the physical case and is also the simplest technically for the above model. The minimizing configuration is always obtained by shrinking the ρ -meson line to zero and connecting sources and currents with pions, that is, the joints coincide with the location of the currents. Thus, for $r \ll T$, $\rho(r) \propto e^{-m_\pi r}$ while for $r \gg T$, $\rho(r) \propto e^{-2m_\pi r}$ since the pions have to go back and forth. The case $\frac{1}{2}m_\rho < m_\pi < m_\rho$ is similar except that it is energetically more favorable for the two pions in the t -channel to combine into a ρ -meson when the angle between them becomes smaller than the critical angle

$$\theta_{\pi\rho} = 2 \cos^{-1} \left(\frac{m_\rho}{2m_\pi} \right) . \quad (3.5)$$

Combining both cases, we conclude that one should observe a transition from $\rho \propto e^{-m_\pi r}$ to $\rho \propto e^{-m_H r}$ where $m_H = \min \{2m_\pi, m_\rho\}$ as r increases from $r \ll T$ to $r \gg T$.

Physically, one should note that the transition from $\rho \propto e^{-m_\pi r}$ to $\rho \propto e^{-m_H r}$ when $r \sim T$ is a lattice artifact and that the true physical result corresponds to the limit $T \rightarrow \infty$. This limit is straightforward to evaluate using the tree level path integral result and thus provides an extremely useful extrapolation tool. In practice, one first calculates the tree level path integral for the actual lattice geometry as done in Fig. 5 to verify consistency with the lattice result. One then recalculates the tree level path integral for $T \rightarrow \infty$, and uses the change in the asymptotic behavior as a correction to the finite lattice result. The

effect of this correction is shown by the dashed lines in Fig. 5 at κ_2 and κ_5 , which show the correct physical asymptotic behavior in the limit $T \rightarrow \infty$.

In principle, the tree diagram path integral analysis is analogous for the ρ and nucleon. However, an interesting new feature arises in the case of the ρ . Naively, one would expect the relevant diagram to be of the form shown in Fig. 4 with all three π 's replaced by ρ 's. However, the operator $\bar{u}\gamma_\mu u \simeq \omega_\mu - \rho_\mu$ does not project onto a physical ρ but rather creates a linear combination of a ρ and ω . The ω component may then couple to a ρ and π , since the effective hadron theory contains a $\pi\omega\rho$ vertex of the form

$$\mathcal{L}_{\pi\omega\rho} = g_{\pi\omega\rho} \partial_\alpha \omega_\beta \partial_\gamma \pi \rho_\delta \epsilon^{\alpha\beta\gamma\delta} \quad (3.6)$$

Hence, there is also a diagram in which ρ 's propagate from the sources to \vec{r}_1 and \vec{r}_2 , ω 's propagate from ρ^u and ρ^d to \vec{r}_1 and \vec{r}_2 , and a π propagates between \vec{r}_1 and \vec{r}_2 . Although $\mathcal{L}_{\pi\omega\rho}$ may be suppressed by the derivative couplings, at sufficiently large $|\vec{r}_1 - \vec{r}_2|$, the pion mass in the propagator will ultimately dominate the asymptotic decay, and we will observe this behavior in the lattice results presented in Section V.

The tree level diagram model also allows one to understand the previously puzzling discrepancy between two calculations of density-density correlation functions in Ref. [6]. One calculation, which we will refer to as projected, integrated $\rho(\vec{x}, \frac{T}{2}) \rho(\vec{x} + \vec{y}, \frac{T}{2})$ over all \vec{x} to project onto zero momentum as in Eq. (3.2). The unprojected calculation used $\rho(0, \frac{T}{2}) \rho(\vec{x}, \frac{T}{2})$ and relied upon the fact that non-zero momentum modes would automatically be suppressed by evolution for sufficiently large imaginary time T .

The argument is simplest in the stationary-phase approximation to the tree level path integral, which we have verified is qualitatively similar to the full numerical integral. The dominant term in the sum Eq. (3.2) arises from $\vec{x} = -\vec{y}/2$. If we compare the resulting string configuration sketched in Fig. 6 (which maximizes Eq. (3.4)) with the one for $\vec{x} = \vec{0}$, one observes an important difference. For small \vec{y} , the minimal configuration arises in both cases from pure π -exchange. Since $m_\pi > m_\rho/2$, ρ -mesons start to develop in both

cases for large \vec{y} . However, in the unprojected case the relevant angles are smaller and the ρ -meson strings therefore develop earlier as shown in the sketch. Hence, we expect that the unprojected correlation function will approach the ρ slope earlier than the projected one, and this expectation is verified in the calculations shown in Fig. 7. This result agrees qualitatively with that presented in Ref. [6] and, we believe, explains the reason for the observed behavior. However, physically, we know that the approach to the ρ slope rather than the π slope is an artifact due to the fact that the extent in T is too small. Thus, the most physical calculation is to perform the projection summation, which significantly suppresses the ρ contributions and then, in addition, correct for the effect of finite T by calculating the difference between the tree diagram path integral with finite T and $T \rightarrow \infty$ as discussed in connection with the dashed curves in Fig. 5.

IV. DETERMINATION OF HADRON PROPERTIES FROM CORRELATION FUNCTIONS ON A LATTICE

In this section we will study density-density correlations on a lattice [12,2]

$$\rho(\vec{y}, t_1, t_2) \stackrel{\text{def}}{=} \sum_{\vec{x}} \langle h_s | (\bar{u}_{\vec{x}, t_2} \gamma^0 u_{\vec{x}, t_2}) (\bar{d}_{\vec{x}+\vec{y}, t_1} \gamma^0 d_{\vec{x}+\vec{y}, t_1}) | h_s \rangle \quad , \quad (4.1)$$

where $|h_s\rangle$ is some superposition of states created by our lattice sources at $t_0 = 0$ and annihilated at $t_3 = T$. Inserting complete sets of states one finds

$$\begin{aligned} \rho(\vec{y}, t_1, t_2) = & \sum_{h_1, h_2, n} \sum_{\vec{p}, \vec{q}} e^{i\vec{q}\vec{y}} C_{\vec{p}, h_2}^* \frac{e^{-(T-t_2)p_{h_2}^0}}{p_{h_2}^0} \\ & \times \langle h_2, \vec{p} | \bar{u} \gamma^0 u | n, \vec{p} + \vec{q} \rangle \frac{e^{-(t_2-t_1)p_n^0}}{p_n^0} \langle n, \vec{p} + \vec{q} | \bar{d} \gamma^0 d | h_1, \vec{p} \rangle \frac{e^{-t_1 p_{h_1}^0}}{p_{h_1}^0} \cdot C_{\vec{p}, h_1} \end{aligned} \quad (4.2)$$

The kinematic factors $p_h^0 = \sqrt{\vec{p}^2 + M_h^2}$, $p_n^0 = \sqrt{(\vec{p} + \vec{q})^2 + M_n^2}$ have been introduced to insure that the states satisfy covariant normalization conditions in the continuum limit. Equation(4.2) is exact, but as it stands, is not very useful because it is too complicated.

In addition to summing over all excitations n in the intermediate state, we have also summed over all excitations of the initial (h_1) and final (h_2) states as well as over all

momenta to which the lattice sources couple, with amplitudes $C_{\vec{p}}$. In this work we will use bag model sources [13] to produce a maximal overlap with the ground state hadrons. However, it is technically impractical to project such localized sources to a fixed momentum such as $\vec{p} = 0$. Since localized sources imply an uncertainty in momentum space, one has to pay a price for physical sources by accepting a convolution over momenta.

In many cases, Eq. (4.2) can be simplified considerably. Although the bag sources imply a convolution in momentum space, the large overlap with ground state hadrons allows one to drop the sum over initial and final state hadrons (provided the currents are not too close to the walls) and one is left with the correlation function in the ground state $|h\rangle$

$$\begin{aligned} \rho(\vec{y}, t_1, t_2) \approx \rho(\vec{y}, t) &= \sum_n \sum_{\vec{p}, \vec{q}} \frac{|C_{\vec{p}}|^2}{p^{02}} e^{-p_0 \cdot T} \\ &\times \langle h, \vec{p} | \bar{u} \gamma^0 u | n, \vec{p} + \vec{q} \rangle \frac{e^{-t(p_n^0 - p^0)}}{p_n^0} \langle n, \vec{p} + \vec{q} | \bar{d} \gamma^0 d | h, \vec{p} \rangle e^{i\vec{q}\vec{y}} \quad , \end{aligned} \quad (4.3)$$

where $p_0 = p_h^0 = \sqrt{\vec{p}^2 + M_h^2}$, $t = t_2 - t_1$. As discussed above, we are *a priori* not allowed to drop the summation over the momentum of the initial/final state.

Let us first consider the simpler equal time case, $t = 0$. In this case, the second moment of the density-density-correlation is related to the size of the hadron. For example, for non-relativistic states one finds

$$\left\langle (\vec{r}_u - \vec{r}_d)^2 \right\rangle \equiv \frac{\sum_{\vec{y}} \vec{y}^2 \rho(\vec{y}, 0)}{\sum_{\vec{y}} \rho(\vec{y}, 0)} = - \sum_n \nabla_{\vec{q}^2}^2 F_{hn}^u(\vec{q}) F_{nh}^d(-\vec{q}) \Big|_{\vec{q}=0} \quad , \quad (4.4)$$

where we have introduced the non-relativistic form factors

$$F_{hn}^u(\vec{q}) = \langle h, \vec{p} | \bar{u} \gamma^0 u | n, \vec{p} + \vec{q} \rangle = \begin{cases} 1 - \frac{R_u^2}{6} \vec{q}^2 + \mathcal{O}(\vec{q}^4) & n = h \\ \vec{q} \cdot \vec{d}_{hn}^u + \mathcal{O}(q^2) & n \neq h \end{cases} \quad , \quad (4.5)$$

and similarly for the down quarks.

Inserting the low \vec{q}^2 expansion of the form factors (4.5) into (4.4) and separating the result into obvious ground state and polarization terms, one thus obtains

$$\langle (\vec{r}_u - \vec{r}_d)^2 \rangle = R_u^2 + R_d^2 - 2 \sum_n \vec{d}_{hn}^u \vec{d}_{nh}^d \equiv 2 \left[\langle r^2 \rangle_{\text{gs}} + \langle r^2 \rangle_{\text{pol}} \right] . \quad (4.6)$$

The origin of the dipole-dipole term, which has been omitted previously [2,4], becomes particularly clear if we rewrite the correlation function in the form

$$\begin{aligned} \langle h | e^{i\vec{q}(\hat{r}_u - \hat{r}_d)} | h \rangle &= \left\langle h \left| 1 - \frac{[\vec{q} \cdot (\hat{r}_u - \hat{r}_d)]^2}{2} \right| h \right\rangle + \mathcal{O}(\vec{q}^4) \\ &= 1 - \sum_n \left\langle h \left| \frac{(\vec{q} \cdot \hat{r}_u)^2}{2} \right| n \right\rangle \langle n | h \rangle \\ &\quad - \sum_n \langle h | n \rangle \left\langle n \left| \frac{(\vec{q} \cdot \hat{r}_d)^2}{2} \right| h \right\rangle \\ &\quad + \sum_n \langle h | \hat{r}_u \cdot \vec{q} | n \rangle \langle n | \hat{r}_d \cdot \vec{q} | h \rangle + \mathcal{O}(\vec{q}^4) , \end{aligned} \quad (4.7)$$

where we have inserted complete sets of states in order to have only single-particle operators appearing. Due to the orthogonality of the states, only $n = h$ contributes in the first two terms and these terms give rise to the ground state rms radius in Eq. (4.6). The last term, however, includes the dipole-dipole transition contributions to the correlation.

Let us now estimate the importance of the $\vec{d} \cdot \vec{d}$ term for nonrelativistic quarks. From the positivity of $\langle (\vec{r}_u \pm \vec{r}_d)^2 \rangle$ one finds the rather crude bounds

$$-\langle r^2 \rangle_{\text{gs}} \leq \langle r^2 \rangle_{\text{pol}} \leq \langle r^2 \rangle_{\text{gs}} . \quad (4.8)$$

For more realistic estimates one has to make some model assumptions. For example, in a non-relativistic two-body problem with equal masses for up and down quarks one finds in the center-of-mass frame $\vec{r}_u = -\vec{r}_d$ and thus

$$\langle (\vec{r}_u - \vec{r}_d)^2 \rangle = 2 (R_u^2 + R_d^2) , \quad (4.9)$$

so that, in terms of our definitions,

$$\langle r^2 \rangle_{\text{pol}} = \langle r^2 \rangle_{\text{gs}} \quad . \quad (4.10)$$

More generally, defining $\sum_{i < j} \langle (r_i - r_j)^2 \rangle = N(N - 1) [\langle r^2 \rangle_{\text{gs}} + \langle r^2 \rangle_{\text{pol}}]$, one finds for an N -body bound state with equal masses and a symmetric coordinate space wavefunction

$$\langle r^2 \rangle_{\text{pol}} = \frac{1}{N - 1} \langle r^2 \rangle_{\text{gs}} \quad . \quad (4.11)$$

In this non-relativistic estimate, for the nucleon $\langle r^2 \rangle_{\text{pol}} = 1/2 \langle r^2 \rangle_{\text{gs}}$ so that neglect of the polarization correction would lead to an overestimate of $\langle r^2 \rangle_{\text{gs}}$ by 50% — certainly not a negligible correction. The decrease of the relative importance of $\langle r^2 \rangle_{\text{pol}}$ with the number of constituents, Eq. (4.11), can be understood easily. For $N \rightarrow \infty$ the motion of two constituents becomes more and more uncorrelated and more accurately described by a mean field, so that $\langle \vec{r}_i \cdot \vec{r}_j \rangle \xrightarrow{N \rightarrow \infty} 0$ for $i \neq j$. Thus, $\langle (\vec{r}_i - \vec{r}_j)^2 \rangle \rightarrow \langle r_i^2 \rangle + \langle r_j^2 \rangle$ for $i \neq j$.

The physical case involves significant corrections to the previous non-relativistic argument. A sizable fraction of the mass can come from the gluons and the center-of-mass of the quarks need not coincide with the center-of-mass of the hadron. One can even imagine an extreme situation, in which the quarks are tightly bound together and move (together) around a large cloud of gluons — thereby yielding a large value for $\langle r^2 \rangle_{\text{gs}}$ while $\langle (\vec{r}_i - \vec{r}_j)^2 \rangle$ remains small — which provides a scenario where one approaches the lower bound in Eq. (4.8). In addition, relativistically, the notion of a center-of-mass is no longer appropriate, since the center-of-mass fluctuates. Although we are unable to provide a realistic estimate for QCD, the importance of the $\vec{d} \cdot \vec{d}$ -term in Eq. (4.6) should be evident.

In a lattice calculation, one would prefer not to rely on model assumptions, so it is helpful to consider density-density correlation functions at unequal times [14]. Neglecting the motion of the center-of-mass for a moment, one finds in the non-relativistic case

$$R^2(t) \equiv \frac{\sum_{\vec{y}} \vec{y}^2 \rho(\vec{y}, t)}{\sum_{\vec{y}} \rho(\vec{y}, t)} = \langle r_u^2 \rangle + \langle r_d^2 \rangle - 2 \sum_n e^{-(E_n - E_h)t} \vec{d}_{hn}^u \vec{d}_{nh}^d \quad . \quad (4.12)$$

Thus the $\vec{d} \cdot \vec{d}$ -terms are exponentially suppressed for large t , which allows one not only to extract $\langle r_u^2 \rangle + \langle r_d^2 \rangle$ in a model independent way but also to extract the off-diagonal elements of the polarizability tensor α_{ud} (where the rows and columns are labeled by flavor indices) from the approach to the asymptotic value by means of

$$\int_0^\infty dt [R^2(t) - R^2(\infty)] = -2 \sum_n \frac{\vec{d}_{hn}^u \vec{d}_{nh}^d}{E_n - E_h} = 2\alpha_{ud} \quad . \quad (4.13)$$

A direct lattice measurement of hadron polarizabilities would be extremely interesting in view of efforts to measure them experimentally [15].

However, as we indicated already above, there are extra complications arising from the motion of the hadron between the two measurements as well as due to relativistic effects.

With*

$$\begin{aligned} & \langle h, \vec{p} \mid \bar{u}\gamma^0 u \mid n, \vec{p} + \vec{q} \rangle \\ &= \begin{cases} \left(\sqrt{\vec{p}^2 + M_h^2} + \sqrt{(\vec{p} + \vec{q})^2 + M_h^2} \right) \left(1 + \frac{R_u^2}{6} q^2 \right) + \mathcal{O}(\vec{q}^4) & n = h \\ \vec{d}_{hn}^u \cdot \vec{q} + \mathcal{O}(\vec{q}^2) & n \neq h \end{cases} \end{aligned} \quad (4.14)$$

where

$$q^2 = \left(\sqrt{\vec{p}^2 + M_h^2} - \sqrt{(\vec{p} + \vec{q})^2 + M_h^2} \right)^2 - \vec{q}^2 = -\vec{q}^2 + \frac{(\vec{p} \cdot \vec{q})^2}{M_h^2 + \vec{p}^2} + \mathcal{O}(\vec{q}^3) \quad , \quad (4.15)$$

one finds for the second moment of the correlation function, after averaging over the angular direction, and omitting terms exponentially suppressed in t :

$$\begin{aligned} R_{\text{rel}}^2(t) &\equiv \frac{\sum_{\vec{y}} \rho(\vec{y}) \vec{y}^2}{\sum_{\vec{y}} \rho(\vec{y})} \\ &= \frac{\sum_{\vec{p}} \frac{2C_{\vec{p}}^2}{E_p} e^{-E_p \cdot T} \left\{ 2(R_u^2 + R_d^2) \left[1 - \frac{\vec{p}^2}{3E_p^2} \right] + \frac{6t}{E_p} \left[1 - \frac{\vec{p}^2}{3E_p^2} \right] - \frac{2t^2 \vec{p}^2}{E_p^2} - \frac{4\vec{p}^2}{E_p^4} \right\}}{\sum_{\vec{p}} \frac{4C_{\vec{p}}^2}{E_p} e^{-E_p \cdot T}} \end{aligned} \quad (4.16)$$

* Here we omit the correct relativistic normalization of \vec{d} since, as we will discuss later, we are not able to determine the polarizability in regimes where relativistic effects become sizable.

where $E_p = \sqrt{\vec{p}^2 + M_h^2} = p_h^0$. A comparison with Eq. (4.12) (non-relativistic approximation and neglect of the motion of the hadron from t_1 to t_2) shows several new effects. First there are some extra relativistic normalization factors such as the factor multiplying R^2 which corresponds to Lorentz contraction. Secondly, the term linear in t arises from the motion of the hadron and reflects retardation effects. The latter are important for the Compton-polarizability of a charged point-like particle [15,16]. Furthermore, there are relativistic recoil terms of order \vec{p}^2/E_p^2 . Most importantly, however, the momentum \vec{p} of the initial state no longer factorizes, which makes it cumbersome to extract rms radii, polarizabilities, and form factors from lattice measurements. For example, the polarizability becomes momentum dependent. The reason is that α_{ud} is defined as the second derivative of the energy M of a particle at rest in a background electric field, in our case $\partial^2 M/\partial\mathcal{E}_u\partial\mathcal{E}_d$, where \mathcal{E}_u and \mathcal{E}_d act on up and down quarks, respectively. Since the electric field is not a Lorentz scalar, hadrons with different momenta \vec{p} experience different polarizabilities. The polarizability even depends on the angle between the momentum \vec{p} and the electric field \vec{E} (this dependence is contained in the \vec{p} -dependence of \vec{d}_{hn} which we have suppressed).

Due to these problems we will not discuss further how to extract the polarizabilities in the general case. Rather, it is clearly preferable to use momentum projected sources — which is a possible extension of this work in some cases — to extract the polarizability, as in the static case, by integrating the exponential term. In practice this is again achieved by integrating the difference between Eq. (4.16) and the full expression for the time dependent density-density correlation function, Eq. (4.3).

We have determined the momentum distribution $C_{\vec{p}}^2$ of our bag sources numerically by calculating the overlap between a localized source and a momentum projected source. Typical calculations show $m^{-2}\langle\vec{p}^2\rangle \equiv m^{-2}\sum_{\vec{p}}C_{\vec{p}}^2\vec{p}^2/\sum_{\vec{p}}C_{\vec{p}}^2$ to be of the order of ten percent or less [17]. These are small enough that using the measured $C_{\vec{p}}$ one could subtract the terms linear and quadratic in t and extrapolate to $t \rightarrow \infty$ in order to eliminate the

exponentially suppressed dipole-dipole terms to obtain the isoscalar rms radii

$$\frac{1}{2} (\langle r_u^2 \rangle + \langle r_d^2 \rangle) = \begin{cases} 2 \langle r_{\text{charge}}^2 \rangle_{\pi^+} & \text{pion} \\ \langle r_{\text{charge}}^2 \rangle_p + \frac{5}{4} \langle r_{\text{charge}}^2 \rangle_n & \text{nucleon} \end{cases} \quad (4.17)$$

Note that we have restricted our attention to u - d correlations for the usual computational reason that all observables can be evaluated using propagators calculated from the bag sources. In the future, u - u and d - d correlations need to be considered as well to disentangle the electromagnetic observables in the proton and neutron [4].

V. LATTICE RESULTS

Monte Carlo calculation

Density-density correlation functions were calculated on $12^3 \times 16$ and 16^4 lattices using 20 quenched $SU(3)$ configurations generated by the Cabillo-Marinari heat bath method [18] with coupling $\beta = \frac{6}{g^2} = 5.7$. For convenience, we have used the value of the lattice spacing determined from the string tension, $a \sim 0.2 \text{ fm}$ with $a^{-1} \sim 1 \text{ GeV}$, with the result that the spatial length of our largest lattice is 3.2 fm. Clearly, for the purpose of comparison with the tree diagram path integral, the precise value of the lattice scale is inessential.

Propagators were calculated at the three values of κ shown in Table 1, for which the lightest pion mass is approximately 340 MeV. All the results shown in this paper used distributed bag model sources [13,19] at the first and last time slices, with hard-wall boundary conditions for the fermions to prevent quark propagation across the time boundary.

The gauge fields were fixed to Coulomb gauge on the source time slices, and the bag radius was set to 1fm. As shown in Ref. [13], the bag sources project onto the hadron ground state extremely effectively, providing in general clean signals and broad plateaus in the number of time slices away from the source. Density operators were averaged over the central four time slices. In order to calculate the effect of momentum projection as

mentioned in Section III, calculations for mesons were also carried out using uniform wall sources instead of bag sources on one time boundary. This, of course, produced significantly less of a plateau region on the wall source side. Analogous calculations for the nucleon were too noisy to be useful because integration over the wall of a third propagator which is not tied to a density operator requires a higher degree of phase cancellation than our present statistics could provide.

Image Correction

As described in section II, the physical correlation function for an isolated hadron is determined by subtraction of the tails of the densities of all first images. The most desirable way to perform this subtraction would be to use the known asymptotic behavior of the correlator, and the tree-level path integral described in this work provides one very attractive means to obtain this behavior. In analyzing the lattice results, however, we have used a self-consistent phenomenological analysis which utilizes only the lattice data itself.

We iteratively improve the image corrections by approximately correcting for images using an appropriately defined parametric curve, least-squares fitting the parameters of the curve to the corrected data, and iterating to self-consistency. In practice, this procedure always yields a smooth, universal curve at large distances, as will be shown in examples below, and is insensitive to the precise form of parameterization. Note also that the iterative procedure is robust and achievement of a universal curve is a strong consistency check of the calculation and parameterization. If the parametric curve were too low, the image correction would be too small, and the corrected data would then be too high and inconsistent with the curve. The parametric curve is thus always driven in the proper direction, and consistency between the final curve and all the corrected data requires correct parameterization of the asymptotic density over a wide range of r . The actual form of the asymptotic density we have used is the following [19]

$$\rho(r) = \rho_0 e^{-m_1 r - g(r)(r-R)(m_2 - m_1)} \quad (5.1a)$$

where

$$g(r) = (1 + e^{-b(r-R)})^{-1} \quad (5.1b)$$

This curve smoothly joins exponential decay with mass m_1 for $r \ll R$ with exponential decay with mass m_2 for $r \gg R$ with the transition occurring in the vicinity of R over a range b^{-1} . This form has the advantage that one can easily select physical starting values and has sufficient flexibility for all the cases of interest in this work.

Results

Figure 8 shows how the self-consistent image correction procedure works in the case of the pion density-density correlation functions. The uncorrected data for a 16^3 spatial lattice are shown in (b). By symmetry arguments, the highest points at $r/a = 8$, $8\sqrt{2}$ and $8\sqrt{3}$ are high by factors of 2, 4, and 8 respectively, and the other data in this regime display comparable finite volume effects. The self-consistent fit to the image corrected data is shown in (c), and one clearly sees that all the data now lie on a single universal curve which is very well fit by the self consistent solid curve specified by Eq. 5.1. Note that this curve is strongly constrained all the way out to the corner of the unit cell corresponding to $8\sqrt{3}$ lattice units or $\sim 2.8fm$. This is the curve that was shown in Fig. 5 and agreed in detail with the tree diagram path integral result. For comparison, the uncorrected lattice data for a 12^3 spatial lattice are shown in (a), and the self-consistent fit to the image corrected data is shown by the dashed line in (c). This lattice is sufficiently small that in addition to the sum of tails of first images, one also observes errors beyond 1fm from interactions with the images. Given the accuracy of the tree level path integral in the region of 1–1.5 fm, even this result on an unphysically small 2.4 fm lattice can be combined with the tree level path integral to accurately describe the whole correlation function.

The results for the pion density-density correlation function at all three values of κ given in Table I are shown in Fig. 9. The solid curves are the self-consistent fits to image corrected data discussed above and have previously been shown in Fig. 5 where they agreed well with the tree level path integral results. For clarity in this and subsequent

graphs, nearby image-corrected lattice data are grouped into bins, and data within each bin are combined to a single value by means of a statistically weighted average of both the ordinates and abscissas. The top plot for κ_2 is thus the binned version of plot (c) of Fig. 8. The main conclusion from the results of this graph is that the self-consistent fits to the image corrected data are accurately determined for all three values of the quark mass. In comparing the lattice results with the slopes for the π and ρ masses, we note that as already seen from the tree diagram results, in this regime the slope has not yet reached the pion slope.

Analogous results for the rho density-density correlation function are shown in Fig. 10. In this case, we note that although one can still obtain a meaningful self-consistent fit, the statistical errors in the lattice data are significantly larger than for the π . The most striking result is that as the quark mass decreases, the slope approaches the slope governed by the pion mass. We already noted in the discussion of the tree diagram analysis that there is a $\pi\omega\rho$ effective coupling which produces a pion exchange diagram, and subject to the limitations of the statistics, these results indicate that the coupling is so strong that it dominates the decay at the separations addressed in this work.

Finally, the results for the nucleon density-density correlation function are shown in Fig. 11. In contrast to the meson results, the plateaus in the number of time slices away from the wall are not always as clear as we would like, and at present, we have no theoretical argument why this problem arises for the nucleon. For κ_2 , the plateaus become ambiguous for $r/a \gtrsim 12$ and, indeed, one notes that the last three points appear systematically high. The problem is so pronounced for κ_5 that we were not sufficiently confident of the result to present it.

The shape of the nucleon correlation function is somewhat different from that of the mesons. Whereas for mesons, a roughly constant asymptotic slope sets in around 1fm, we note that only in the vicinity of 2 fm does the nucleon slope begin to turn over and approach the rho slope. Physically, it is plausible that the three-quark core of the nucleon is more extended than the quark-antiquark component of the mesons, so that when the finite size of the relevant vertices is taken into effect, the tree diagrams only begin to describe the asymptotic slope at substantially larger distances.

VI. SUMMARY, CONCLUSIONS, AND OUTLOOK

In this work we have analyzed and performed measurements of correlation functions to study the pion, the rho and the nucleon. Our most important results are the development and successful testing of a scheme to correct systematically for images on periodic lattices, and the development of a tree level path integral to determine the asymptotic behavior of correlation functions. Furthermore, we have clarified the relation between the second moment of density-density correlators and the rms radii of hadrons.

We have shown that as long as the interaction between hadrons and their images in adjacent unit cells is not too large, the difference between lattice gauge theory results for the density-density correlation function on a periodic lattice and an infinitely large lattice is simply due to superposition of the tails of the same correlation function arising from mirror images. In a similar situation in a non-gauge theory, non-diagonal interference terms between wave functions in adjacent cells would also contribute to the density-density correlations. In a gauge theory such interference terms are proportional to Wilson loops enclosing the periodic lattice and thus have the topology of Polyakov lines which are strongly suppressed. We have thus developed a practical method to use the long distance behavior of the density-density correlations on an infinite lattice to correct for the images on a finite volume lattice, and have demonstrated its effectiveness in an explicit lattice calculation.

QCD at large distances can be most effectively described using hadronic degrees of freedom. As a model for the long distance behavior we have employed tree level diagrams, including only the lightest hadron in each channel. For the vector current correlations measured in this work, this is equivalent to vector meson dominance. We have used this model to calculate the asymptotic behavior of the same correlators we have treated on the lattice, and observe good agreement between self-consistent fits to the lattice data and predictions based on our tree level hadron model. This model also makes it clear why the large distance behavior of density-density correlations is not a simple exponential: since

the hadron propagates between the two vector meson vertices, in addition to the mass scale corresponding to the vector meson mass, the mass scale of the hadron itself is also relevant. We have also shown that when the density-density correlation is measured at spatial separations that are comparable to the temporal extent of the lattice, there are further nontrivial r-dependencies arising from incomplete momentum projection due to the finite extension of the lattice in the Euclidean time direction. An important practical result of this work is that because the most important finite size effects in the region $r > 1.5$ fm are now understood, one can be confident of future measurements of correlations on the present physical volumes.

Nonrelativistic arguments suggest a direct relation between the second moment of the density-density correlators and the rms radius, as defined by the slope of the form factor. This result arises because, nonrelativistically, the center of mass of the quarks separates and thus the contribution to the density-density correlation from dipole transitions in the intermediate state between the two current insertions is itself proportional to the rms radius. Unfortunately, this argument does not apply when the quarks are relativistic and the relation between the second moment of the density-density correlation and the rms-radii contains an *a priori* unknown dipole-dipole term.

In this work we have only considered density-density correlations measured at equal time. In future work, it would be desirable to perform measurements of density-density correlations at unequal times for several reasons. By measuring the dependence of the second moment on the time difference, one could extract the polarizability of the hadron which is physically interesting and is being studied experimentally [15,16]. In addition, for sufficiently large times between the two current insertions, the dipole-dipole contributions arising from excited intermediate states are suppressed and only the contribution from the rms radius survives in the second moment.

ACKNOWLEDGEMENTS

The lattice calculations were performed at the National Energy Research Supercomputer Center under an allocation by the D.O.E. This work is supported in part by funds provided by the U.S. Department of Energy under contracts DE-FG06-90ER40561, DE-FG06-88ER40427, and DE-FC02-94ER40818.

APPENDIX A

Density-Density Correlations for General Currents and Dirac Particles

When we derived the large t -behavior of the second moments of the density-density correlation functions we factored the current matrix elements into the invariant form factor and a kinematic piece ($q = p' - p$)

$$\langle p' | \bar{u} \gamma^0 u | p \rangle = F_u(q^2) \cdot (p^0 + p'^0) \quad . \quad (\text{A.1})$$

Of course, for other currents one must use different kinematic factors. For example,

$$\langle p' | \bar{u} \vec{\gamma} u | p \rangle = F_u(q^2) (\vec{p} + \vec{p}') \quad (\text{A.2})$$

or

$$\langle p' | \bar{u} u | p \rangle = F_u^s(q^2) \quad , \quad (\text{A.3})$$

where F_u and F_u^s are the vector and scalar up quark form factors of the hadron. Using these currents, the general structure of the terms appearing in the moments of the correlation functions will be very similar to Eq. (4.16), although the coefficients will be different. For example, for $t = (t_2 - t_1)$

$$\rho_{ii}(\vec{y}, t) = \sum_{\vec{x}, i} \langle h | \bar{u} \gamma^i u(\vec{x} + \vec{y}, t_2) \bar{d} \gamma^i d(\vec{x}, t_1) | h \rangle \quad (\text{A.4})$$

one finds

$$Q_{ii} \equiv \sum_{\vec{y}} \rho_{ii}(\vec{y}, t) = \sum_{\vec{p}} \frac{4C_{\vec{p}}^2}{E_p^3} e^{-E_p \cdot T} \vec{p}^2 \quad (\text{A.5})$$

and

$$\begin{aligned} R_{ii}^2 \equiv \sum_{\vec{y}} \vec{y}^2 \rho_{ii}(\vec{y}, t) &= \sum_{\vec{p}} \frac{2C_{\vec{p}}^2}{E_p^3} e^{-E_p \cdot T} \\ &\times \left\{ 2\vec{p}^2 (R_u^2 + R_d^2) \left(1 - \frac{\vec{p}^2}{3E_p^2} \right) - 3 + 2 \frac{\vec{p}^2}{E_p^2} \left[5 - \frac{3\vec{p}^2}{E_p^2} \right] + 2 \frac{t\vec{p}^2}{E_p} \left[5 - 3 \frac{\vec{p}^2}{E_p^2} \right] - 2 \frac{t^2 \vec{p}^4}{E_p^2} \right\} \end{aligned} \quad (\text{A.6})$$

where as usual, terms exponentially suppressed in t have been omitted. Since the $C_{\vec{p}}$'s, as well as the isoscalar rms Eq. (4.17), can be determined independently, one can actually test Eqs. (A.5) and (A.6) by measuring Q_{ii} and R_{ii}^2 independently. This provides a test of the Lorentz invariance which we have used throughout the derivations. Due to the coarse-grained structure of the lattice at short distances, Lorentz invariance is not guaranteed and it will indeed break down at some point for sufficiently large momenta. Testing Eqs. (A.5) and (A.6) is therefore useful to justify the Lorentz invariance assumption made in the text for “typical” momenta.

We now consider the case of nucleon form factors. Here we will assume $\vec{p} = 0$ in the initial state. In practice this means that one neglects terms of order \vec{p}^2/M^2 in the form factor. Since typical nucleon momenta in a lattice calculation are non-relativistic, this is a reasonable approximation. In fact, for non-relativistic nucleons $\vec{p}^2/2M$ is of the order $1/T$. Hence \vec{p}^2/M^2 is of the order $2/MT \approx 0.1$, where we used $M \approx 1.2 a^{-1}$, $T = 16 a$ as typical values.

Introducing invariant form factors via Refs. [20], [21]

$$\langle p' | \bar{u} \gamma^\mu u | p \rangle = \bar{u}(p') \left[\gamma^\mu F_1^u(q^2) + \frac{i \sigma^{\mu\nu} q_\nu}{2M} F_2^u(q^2) \right] u(p) \quad (\text{A.7})$$

and using

$$F_1^u(q^2) = F_1^u(0) + R_u^2 \frac{q^2}{6} + \mathcal{O}(q^4) \quad (\text{A.8a})$$

$$\mu_u = \frac{1}{2M} [F_1^u(0) + F_2^u(0)] \quad , \quad (\text{A.8b})$$

as well as similar expressions for down quarks, one obtains for spin-1/2 particles

$$\begin{aligned} \frac{\sum_{\vec{y}} \vec{y}^2 \rho(\vec{y}, t)}{\sum_{\vec{y}} \rho(\vec{y}, t)} &= F_1^d(0) (R_u^2 + \frac{3}{M} \mu_u) + F_1^u(0) (R_d^2 + \frac{3}{M} \mu_d) + F_1^u(0) F_1^d(0) \left(\frac{3t}{M} - \frac{3}{2M^2} \right) \\ &\quad - 2 \sum_n e^{-(E_n - E_h)t} \vec{d}_{hn}^u \vec{d}_{nh}^d \quad . \end{aligned} \quad (\text{A.9})$$

Note that for γ_u^0 currents the magnetic matrix elements in Eq. (A.7) are already of order \vec{q}^2 , *i.e.* they do not contribute to inelastic transitions. Hence the polarization terms in (A.9) are purely electric and their time integral yields the u - d matrix element of the electric polarizability.

The magnetic moments enter the expression for the second moment similar to the ground state rms radii. This is reminiscent of the Sachs form factor where also linear combinations of F_1 and F_2 appear [21]. The term linear in t enters with the same coefficient as for spinless hadrons. This should not be surprising, since it arises from the classical acceleration of the charged particle in an external electric field. Similar to the mesonic case, this term even survives for point-like particles. For Dirac particles ($R^2 = 0$, $\mu = 1/2M$) the result still differs from point-like scalars and a finite “effective rms” — arising from the spin — remains.

Of course, the non-relativistic approximation in (A.9) is not really necessary, although, as we discussed in the context of spinless fields, the polarizability becomes rather difficult to determine. For the second moment, again omitting terms exponentially suppressed in t , one finds

$$\begin{aligned}
\frac{\sum_{\vec{y}} \vec{y}^2 \rho(\vec{y}, t)}{\sum_{\vec{y}} \rho(\vec{y}, t)} &= \left(\sum_{\vec{p}} \frac{4\vec{C}_{\vec{p}}^2}{E_p} e^{-E_p \cdot T} \right)^{-1} \\
&\times \sum_{\vec{p}} \frac{2\vec{C}_{\vec{p}}^2}{E_p} e^{-E_p \cdot T} \left\{ 2 (F_1^d(0)R_u^2 + F_1^u(0)R_d^2) \left(1 - \frac{\vec{p}^2}{3E_p^2} \right) \right. \\
&\quad + F_1^u(0)F_1^d(0) \left[\left(\frac{3}{E_p^2} + \frac{6t}{E_p} \right) \left(1 - \frac{\vec{p}^2}{3E_p^2} \right) - \frac{2t^2\vec{p}^2}{E_p^2} \right] \\
&\quad \left. + \frac{3}{E_p^2} [F_1^d(0)F_2^u(0) + F_1^u(0)F_2^d(0)] - \frac{2\vec{p}^2}{E_p^2 M^2} F_2^u(0)F_2^d(0) \right\}
\end{aligned} \tag{A.10}$$

The only new term in (A.10) is the term quadratic in the magnetic moment — indicating a double spin-flip contribution to the correlation function.

REFERENCES

1. K. Barad, M. Ogilvie and C. Rebbi, *Phys. Lett.* **B143** (1984) 222; *Ann. Phys. (NY)* **168** (1986) 284.
2. W. Wilcox, *Nucl. Phys. B (Proc. Suppl.)* **20** (1991) 459; W. Wilcox and K.-F. Liu, *Phys. Lett.* **B172** (1986) 62; W. Wilcox, *Phys. Rev.* **D43** (1991) 2443.
3. M.-C. Chu, M. Lissia and J. W. Negele, *Nucl. Phys.* **B360** (1991) 31.
4. M.-C. Chu, M. Lissia, J. W. Negele, and J. M. Grandy, *Nucl. Phys. A* **555** (1993) 272.
5. Lattice 93 — Teo... “The definition and lattice measurement of hadron wave functions,” submitted to Proceedings of Lattice ’93 (Dallas, TX)...
6. W. Wilcox, *Nucl. Phys. B (Proc. Suppl.)* **26** (1992) 491.
7. N. S. Manton, *Ann. Phys. (NY)* **159** (1985) 220; J. E. Hetrick and Y. Hosotani, *Phys. Rev.* **D38** (1988) 2621; F. Lenz, M. Thies, S. Levit and K. Yazaki, *Ann. Phys. (NY)* **208** (1991) 1.
8. J. Kogut and L. Susskind, *Phys. Rev.* **D11** (1974) 395.
9. S. Huang, J. W. Negele, and J. Polonyi, *Nucl. Phys.* **B307** (1988) 669.
10. R. L. Jaffe and P. Mende, *Nucl. Phys. B* **369** (1992) 189.
11. M. Creutz, *Quarks, Gluons and Lattices* (Cambridge University Press, Cambridge, UK, 1983), p. 17.
12. W. Wilcox and K.-F. Liu, *Phys. Rev.* **D34** (1986) 3882.
13. M.-C. Chu, J. M. Grandy, M. Lissia and J. W. Negele, *Nucl. Phys. B (Proc. Suppl.)* **26** (1992) 412.
14. W. Wilcox, *Phys. Lett.* **B289** (1992) 411; *ibid.* *Nucl. Phys. B (Proc. Suppl.)* **30** (1993) 491.

15. F. J. Federspiel *et al.*, *Phys. Rev. Lett.* **67** (1991) 1511; J. Schmiedmayer *et al.*, *Phys. Rev. Lett.* **66** (1991) 1015; B. R. Holstein, *Comm. Nucl. Part. Phys.* **19** (1990) 221.
16. H. R. Fiebig, W. Wilcox and R. M. Woloshyn, *Nucl. Phys.* **B234** (1983) 47.
17. K. Teo, Ph.D. Thesis, Massachusetts Institute of Technology, 1994, unpublished.
18. N. Cabibbo and E. Marinari, *Phys. Lett.* **B119** (1982) 387.
19. J. M. Grandy, Ph.D. Thesis, Massachusetts Institute of Technology, 1992, unpublished.
20. C. Itzykson and J.-B. Zuber, *Quantum Field Theory* (McGraw-Hill, Singapore, 1985).
21. D. B. Leinweber, R. M. Woloshyn and T. Draper, *Phys. Rev.* **D43** (1991) 1659.

FIGURE CAPTIONS

Fig. 1: Density-density correlation for non-relativistic positronium in QED_{1+1} on a lattice with $N = 10$ sites and periodic boundary conditions. The heavy solid curve shows the periodic solution on a circle and the dashed curve denotes the image corrected result. For comparison the result for an open line ($N \rightarrow \infty$) is shown by the light solid curve, and this solution displaced by $\pm L$ is shown by the dotted curves to indicate the degree of overlap.

Fig. 2: Fourier transforms of the density-density correlation functions shown in Fig. 1. The solid points denote the Fourier transform of the periodic density at the discrete lattice momenta $p_\mu = \frac{2\pi k}{L}$ and the dashed curves show the Fourier transform of the solution on the open line. The solid curve in (a) shows the result of using the asymptotic form Eq (2.18) with b/a chosen to make the second derivative continuous, and the solid curve in (b) shows the errors introduced by a discontinuous second derivative arising from Eq. (2.16). The solid curves in (c) are obtained as in case (a) from an ensemble of ten data sets in which the periodic solution has been modulated with 1% relative random noise.

Fig. 3: Time histories contributing to meson density-density correlation functions with periodic boundary conditions in the spatial direction. The sources creating the meson are denoted by the solid dots on the Euclidean time boundaries and the density operators are represented by the interior solid dots. Quark propagators on the front and back surfaces of the cylinder are denoted by solid and dashed wiggly lines respectively.

Fig. 4: Space-time diagrams for $\langle \rho_u \rho_d \rangle$. The left sketch shows a typical time-history in the quenched approximation, with quark propagators denoted by wiggly lines. The sketch on the right shows the corresponding tree-level graph at large separations in which the pairs of $q\bar{q}$ propagators and the associated gluons are replaced by ground state meson propagators.

Fig. 5: Comparison of approximations to the pion density-density correlation function $\rho(r)$ at large separation r . The sum of all tree-level diagrams without image corrections is given by the open squares. Image corrected results at the symmetry points are shown by solid octagons and interior points with negligible image corrections are indicated by solid squares. The best fit to the image corrected lattice QCD results is denoted by the solid curves and for comparison, the pion and rho slopes are shown by dotted lines. The dashed lines indicate the corrected asymptotic behavior obtained by taking the $T \rightarrow \infty$ limit of the tree diagrams as discussed in the text. The three values of the hopping parameter κ correspond to the masses given in Table I. The distance is calibrated both in lattice units (lower scale) and fm assuming $a=0.2\text{fm}$ (upper scale).

Fig. 6: Space-time diagrams for the pion $\langle \rho_u \rho_d \rangle$ in the stationary tree-level approximation. The upper and lower graphs correspond to small and large spatial separations respectively. The left graphs correspond to the configurations in which the summand in Eq. (3.4) is maximal and the right graphs represent the non-summed geometry. Note the appearance of a ρ propagator in d.

Fig. 7: Comparison between the stationary tree-level approximation to the pion $\langle \rho_u \rho_d \rangle$ in the unprojected (full line) and the projected (dashed line) cases for relative separation r . For reference, the slopes corresponding to $m_\pi = 0.33$, and $m_\rho = 0.615$ are given by the dotted lines.

Fig. 8: Lattice results for pion density-density correlation functions with and without image corrections. Uncorrected results with statistical errors on 12^3 and 16^3 spatial lattices are shown in (a) and (b) respectively, shifted by a decade for clarity. Shifted by an additional decade, the self-consistent fit to the asymptotic density for the 16^3 lattice using Eq. (5.1) is shown by the solid line in (c), along with the image corrected lattice data using this fit. For comparison, the dashed line in (c) shows the analogous self-consistent fit obtained from the $(12)^3$ data. All results are for the hopping parameter

κ_2 of table I. The radial distance is shown in lattice units on the bottom scale and in fm on the top scale.

Fig. 9: Image corrected pion density correlation functions at the three values of κ given in Table I. For clarity, the data have been aggregated into bins, and each correlation function is shifted by 3 decades. As in Fig. 8, the solid curves denote the self-consistent fits and the error bars denote the image-corrected lattice measurements. For reference, the slopes corresponding to m_π and m_ρ given in Table I for the corresponding κ are denoted by dotted lines. The radial distance is shown in lattice units on the bottom scale and in fm on the top scale.

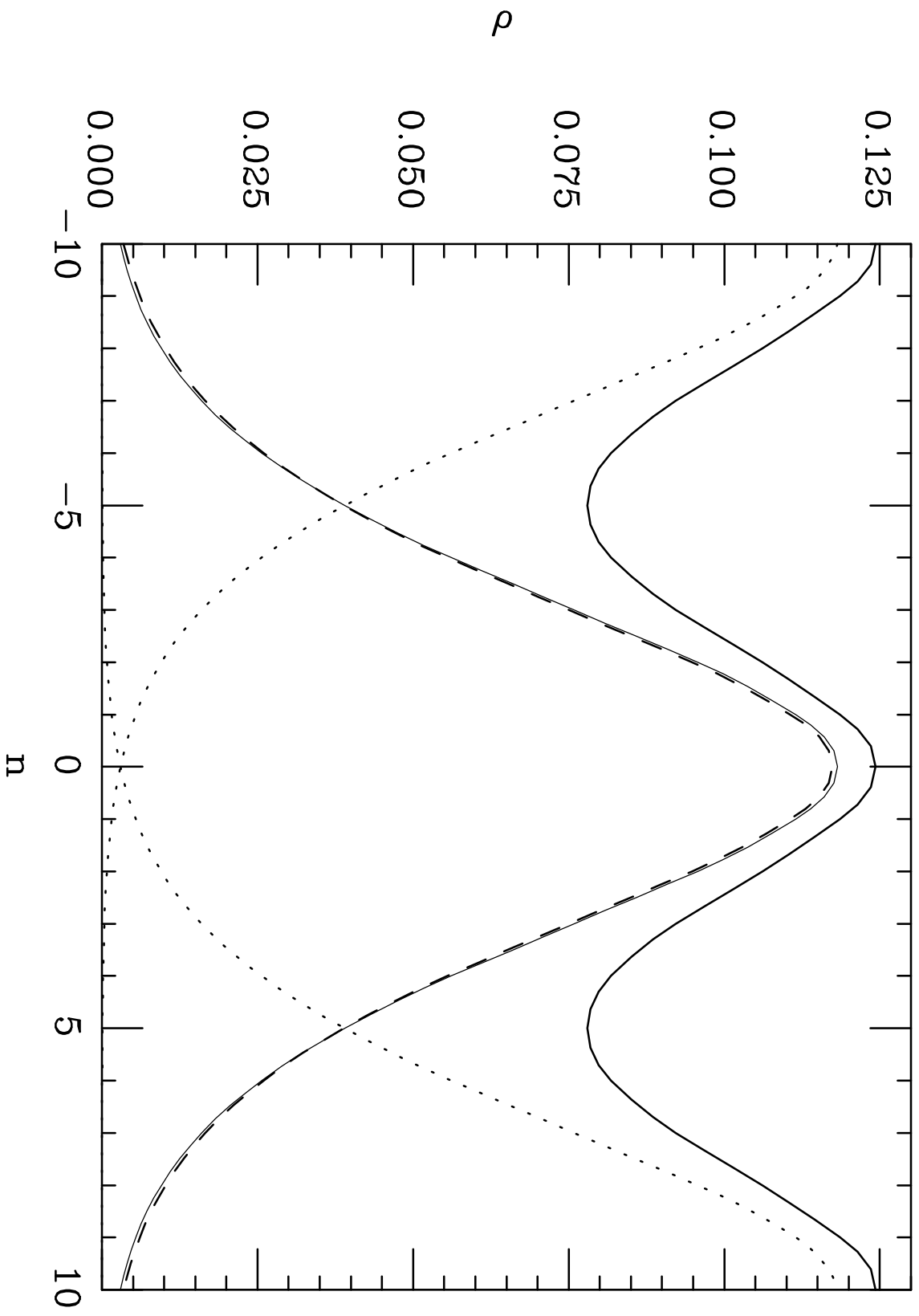
Fig. 10: Image corrected rho density-density correlation functions. The presentation and notation are the same as in Fig. 9.

Fig. 11: Image corrected nucleon density-density correlation functions. The presentation and notation are the same as in Fig. 9.

TABLES

Table I. Hadron masses at the three values of the hopping parameter κ used in the lattice calculations. For reference, a bare quark mass $m_{\hat{q}} = \frac{1}{2\kappa} - \frac{1}{2\kappa_c}$ is also tabulated. The inverse lattice spacing is $a^{-1} = 1$ GeV.

	κ	m_q (MeV)	m_π (MeV)	m_ρ (MeV)	m_N (MeV)
κ_2	0.16	175	691 (3)	813 (4)	1321 (10)
κ_4	0.1639	95	511 (5)	698 (5)	1097 (11)
κ_5	0.167	40	340 (7)	615 (6)	915 (16)



This figure "fig1-1.png" is available in "png" format from:

<http://arxiv.org/ps/hep-lat/9406009v1>

This figure "fig2-1.png" is available in "png" format from:

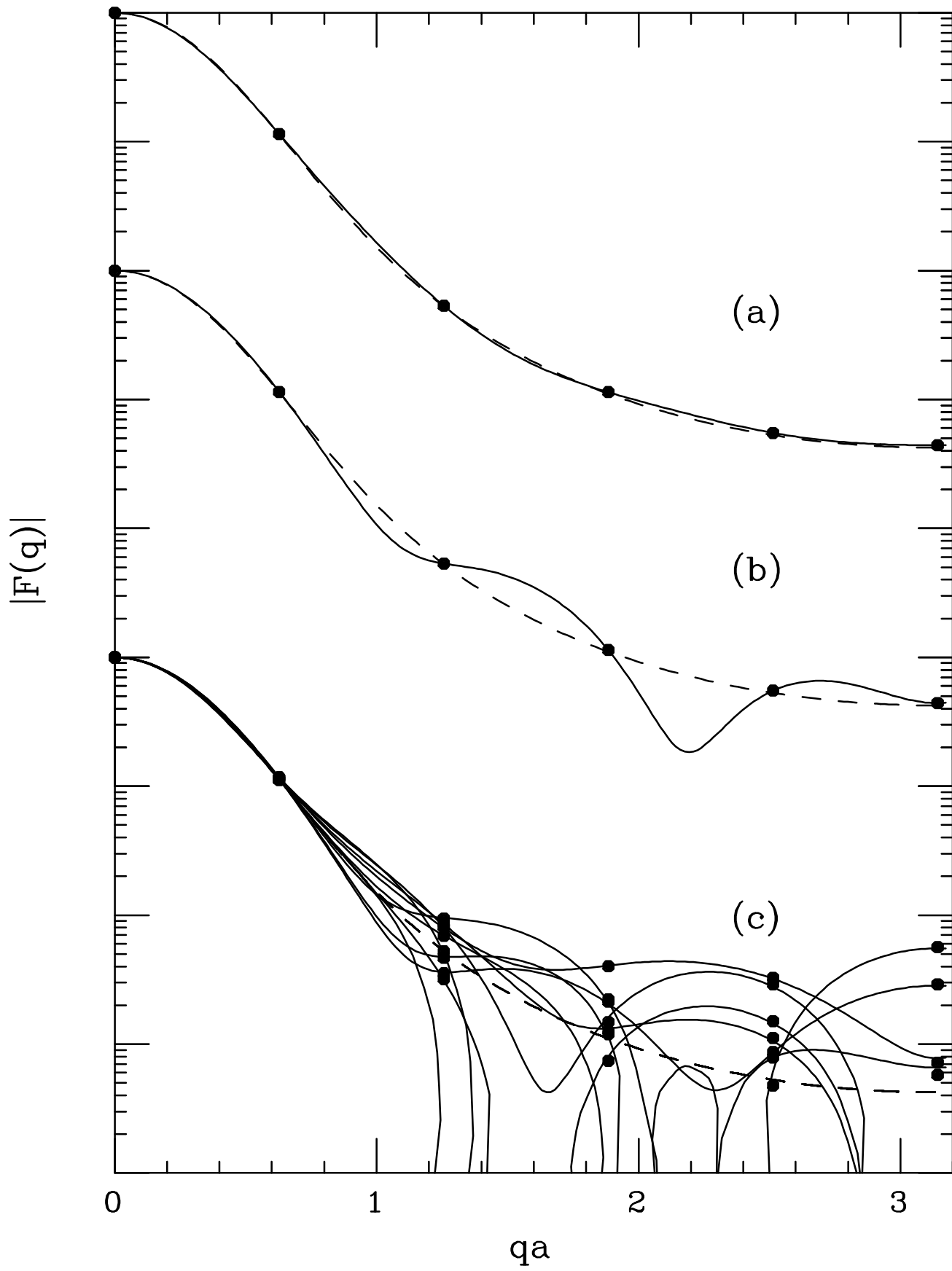
<http://arxiv.org/ps/hep-lat/9406009v1>

This figure "fig3-1.png" is available in "png" format from:

<http://arxiv.org/ps/hep-lat/9406009v1>

This figure "fig4-1.png" is available in "png" format from:

<http://arxiv.org/ps/hep-lat/9406009v1>



This figure "fig1-2.png" is available in "png" format from:

<http://arxiv.org/ps/hep-lat/9406009v1>

This figure "fig2-2.png" is available in "png" format from:

<http://arxiv.org/ps/hep-lat/9406009v1>

This figure "fig3-2.png" is available in "png" format from:

<http://arxiv.org/ps/hep-lat/9406009v1>

This figure "fig4-2.png" is available in "png" format from:

<http://arxiv.org/ps/hep-lat/9406009v1>

This figure "fig3-3.png" is available in "png" format from:

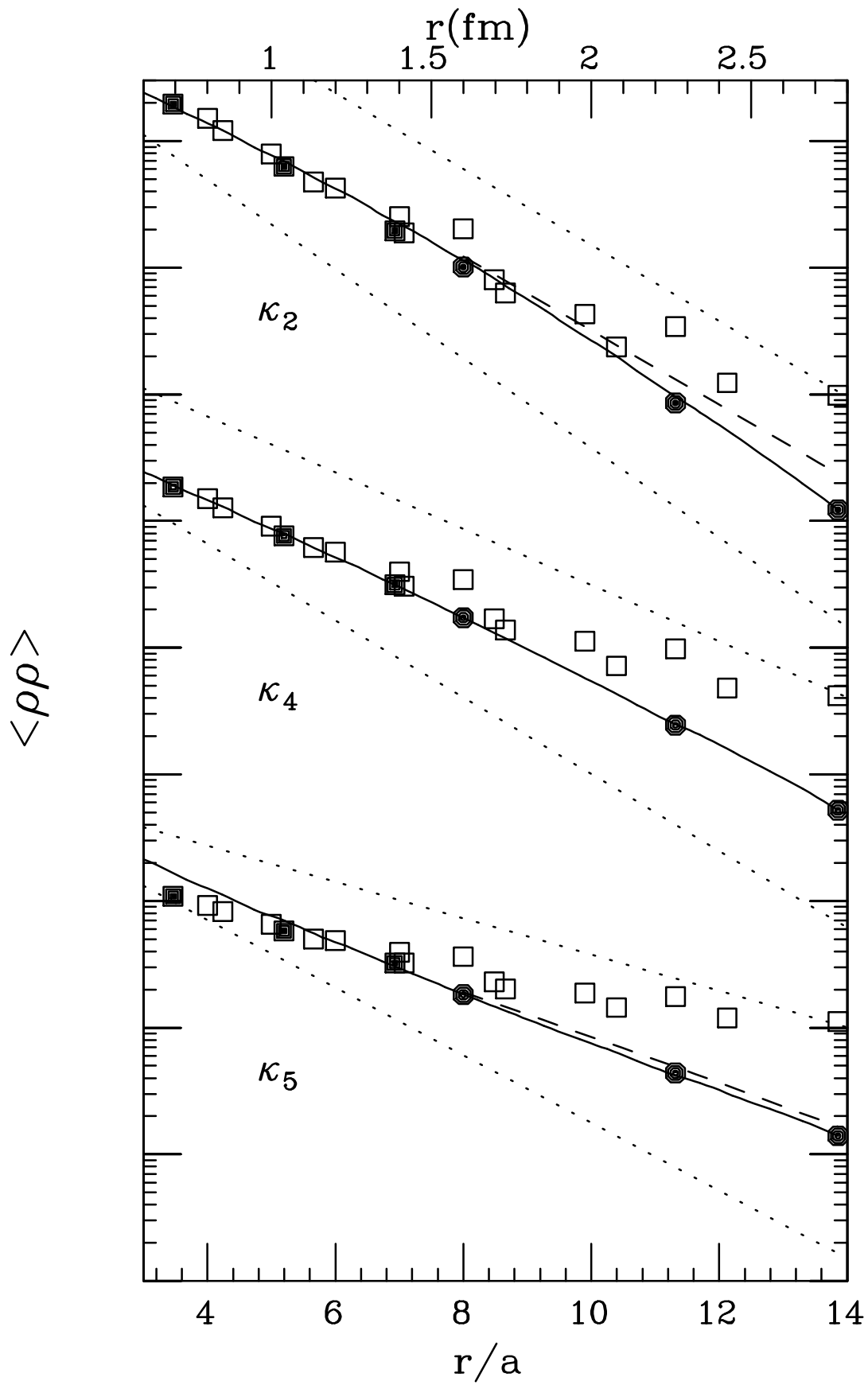
<http://arxiv.org/ps/hep-lat/9406009v1>

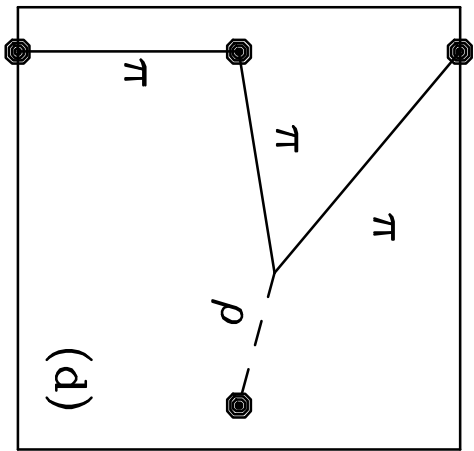
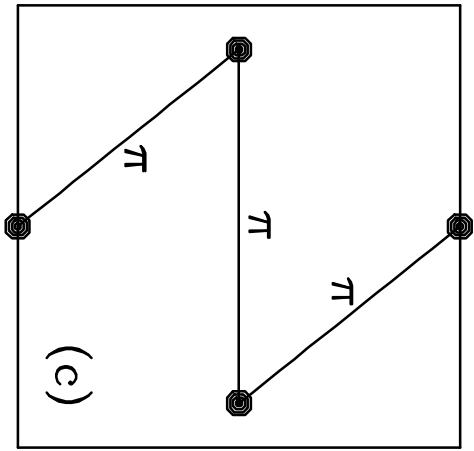
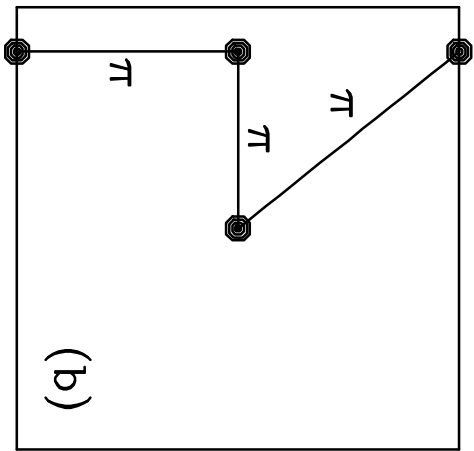
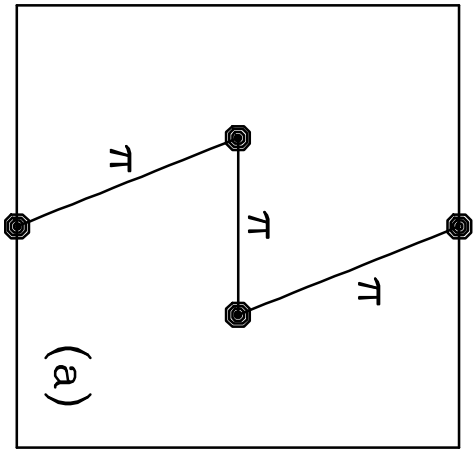
This figure "fig4-3.png" is available in "png" format from:

<http://arxiv.org/ps/hep-lat/9406009v1>

This figure "fig3-4.png" is available in "png" format from:

<http://arxiv.org/ps/hep-lat/9406009v1>





t

t

y

y

$\langle \rho\rho \rangle$

